Chapter-2

Synthesis and characterizations of individual nanoforms of TiO_2 and carbon

2.1 Introduction

Metal oxides having a lot of benefits like simple working principle, non-toxicity, low cost and long-term stability etc. are being reported for different applications [1]. Exemplary electronic exchange characteristics and wide band gap of metal oxide nanoforms make them a superior choice over other nanomaterials [2]. Several metal oxides like SnO_2, WO_3, FeO_3, ZnO, CuO, TiO_2 etc. with a lot of potential have been implied in different domains like photocatalysis [3], biosensors [4], solar cells [5], antibacterial [6], chemical sensors [7], water splitting [8].

TiO_2 is considered as an promising metal oxide for various applications because of its nontoxic nature, long term thermal stability and chemical inertness [9]. TiO_2 is one the important metal oxide semiconductor that is less explored in comparison to SnO_2 and ZnO and also holds on to the good physical and chemical properties. TiO_2 has an advantage to be synthesized and implemented in different nanoforms such as nanotube, nanoparticle, nanorod, nanofiber and nanosphere etc. Various researchers have utilized the unique TiO_2 nanostructures for different applications like water purification [10], photocatalysis [11], photonic crystals [12], gas sensing [13], solar water splitting [14] and supercapacitors [15] etc.

TiO_2 can be fabricated by various low-cost techniques such as sol-gel template [16], surfactant directed [17], hydrothermal [18],[19], anodization of Ti foil [20] etc. 1-D TiO_2 nanostructures can be fabricated using hydrothermal method [21] and anodization of Ti foil [22]. 2-D TiO_2 nanostructures can be synthesized by atomic layer deposition. Zero dimensional TiO_2 nanoparticles can be fabricated using sol-gel method. TiO_2 has the capability to be synthesized in different nanoforms with different nanostructures according to the required application.

Different nanoforms having different dimensions (0-D, 1-D, 2-D and 3-D) have unique advantages. One dimensional nanostructure like nanotubes, nanorods, nanowires have various unique properties like high surface to volume ratio, good stability with uniformity, homogenous structure, adequate dispersion high crystallinity, predefined conductance and eminent resistance etc. [23],[24]. Zero-dimensional (0-D) nanomaterial is one of the most promising material with its unique nature. Excessive small size with highly functioning edge

sites per unit mass and also the quantum confinement effect of 0-D materials makes them supreme among other nanomaterials [25]. 1-D TiO_2 nanotube array have found to be superior among all due to outstanding properties like high surface to volume ratio, one dimensional electron flow and highly crystalline nature [26-28].

Carbon constitutes an important section of nature. Acquainted with the popularity of graphite and diamond which are highly explored and applied in different fields. The new emerging nanocarbons graphene, carbon nanotubes and fullerene have given researchers a lot of opportunities in almost every domain of nanoscience. The semiconductor characteristics and appropriate dimensions of carbon nanostructures makes them a one of perfect nanomaterial in nanotechnology. The excellent chemical and electrical properties of graphene, CNT and fullerene with unique structures, e.g. immense electron mobility, high specific area and small size makes them a adequate candidate for different applications [29],[30].

This chapter includes the detailed synthesis procedure of both TiO_2 nanostructures with their characterization techniques. 1-D TiO_2 nanotubes were fabricated by electrochemical anodization and 0-D TiO_2 nanoparticles were fabricated by sol-gel method. Morphological, structural, chemical characterizations were performed to analyse the TiO_2 nanostructures. The procedure for the formation of graphene oxide solution and fullerene aqueous solution has been described in this chapter along with different characterization techniques (FESEM, TEM, Raman, UV-vis and XPS).

2.2 TiO_2 nanotubes: 1-D material

2.2.1 Synthesis

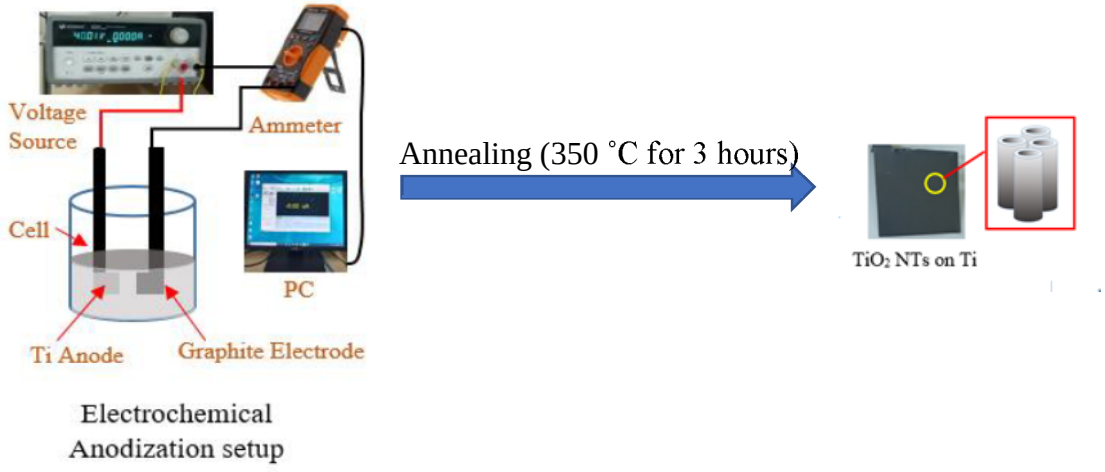

Fig.2.1. TiO_2 nanotube synthesis via electrochemical anodization route.

Highly aligned TiO_2 nanotubes array was synthesized by anodic oxidation route (Fig. 2.1). High purity Ti foil (99% pure, 0.25 mm thick) was cut into 1 cm × 1 cm pieces to be used as an anode material. Ti foil was cleaned with acetone and dried in air for further use. A rectangular-shaped graphite sheet with dimensions 1.5 cm × 1.5 cm (thickness: 1 mm) was used as the counter electrode (cathode). A separation of 3.5 cm was maintained between anode and cathode during anodic oxidation. Anodization was performed at room temperature (300 K) for 90 min under a constant potential of 40-50 V. The electrolyte was prepared with 0.5 wt% of ammonium fluoride (NH_4F), 10 vol% of deionized (Milli-Q) water and ethylene glycol. TiO_2 nanotubes/Ti samples were cleaned with water and ethanol and then dried in air. After that, all the prepared samples were annealed in dry air at 350 °C for 3 h to make the nanotubes electrically stable and robust.

2.2.2 Characterizations

Morphological characterizations

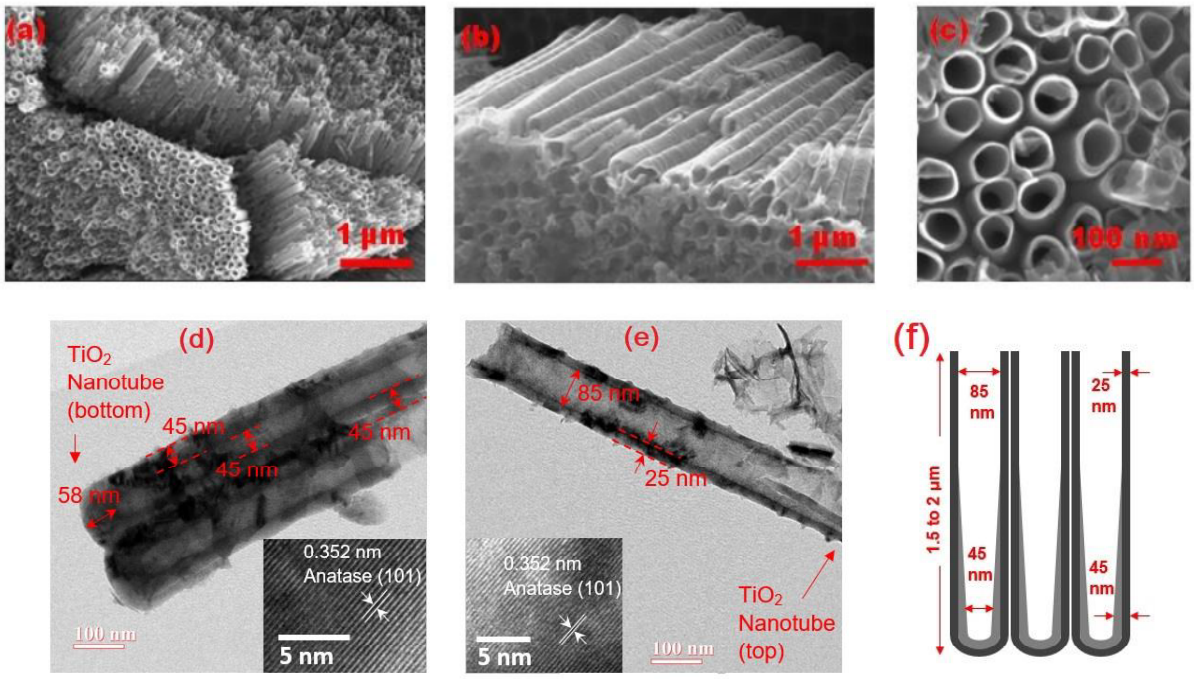

Fig.2.2. FESEM image of TiO_2 nanotubes:(a) overall view of TiO_2 nanotubes (b) top view; (c) side veiw. Corresponding TEM image of (d) bottom and (e) top of the nanotubes. (f) A schamatic of TiO_2 nanotubes with all the essential dimentions is drown based on the TEM results.

Highly arranged and oriented nanotubes were formed by the process of electrochemical anodization. The average length of nanotubes formed is 1.5 - 2 µm. The average outer and inner diameter of the TiO_2 nanotubes were measured as 120-140 nm and 75-90 nm respectively

(Fig.2.2(c)). To further investigate the morphology of nanotubes, TEM was performed (Fig. 2.2 (d) and (e)). TEM image in Fig.2.2(d) and (e) confirm that the wall thickness and inner diameter of anodically grown TiO_2 nanotube are not uniform rather the wall thickness is increased towads bottom direction lowering the inner radius. Wall thickness of TiO_2 nanotubes was measured near bottom and top as 45 nm and 25 nm, respectively.The inner diameter was measured near bottom and top as 45 nm and 85 nm, respectively. Therefore, the outer diameter was almost constant (~135 nm) throughout the length of the nanotube (Fig. 2.2(d) and (e)). As the TEM image is represented by part in Fig. 2.2(d) and (e), a possible schamatic of a complete TiO_2 nanotubes is shown in Fig. 2.2(f) indicating all the essential dimensions. Inter-planar distances of 0.352 nm is corresponding to anatase tetragonal (1 0 1) plane is clearly observed from the insets of the Fig. 2.2 (d) and (e) [31].

Structural characterization

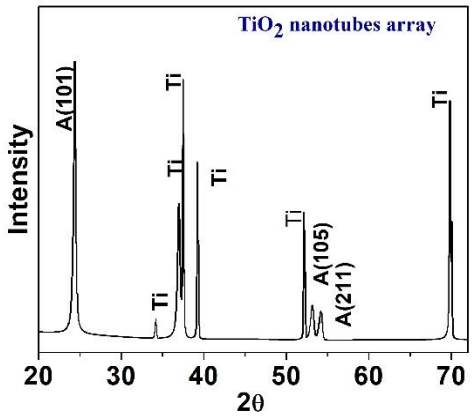

Fig 2.3. XRD spectra of TiO_2 nanotubes.

XRD confirmed the anatase crystallinity of TiO_2 nanotubes (Fig. 2.3). The sharp and high intensity peak at 24.5° corresponds to the A (101) crystallinity. The low intensity peaks at 53.2° and 54.1° correspond to the anatase (105) and (211) respectively. All the other peaks labelled as Ti depicts titanium substrate. The XRD peaks for anatase TiO_2 were authenticated by JCPDS file No. 21-1272.

Other characterizations like Photoluminescence (PL), Raman and UV vis spectroscopy were also performed for the TiO_2 nanotube array (Fig.2.4). PL spectrum was recorded by using a 325 nm laser at room temperature (Fig. 2.4 (a)). PL spectrum exhibited two major peaks – B peak in the UV region (390 nm) and G peak in the visible region. The B peak represents the band-to-band emission i.e. the electronic transition from conduction band to valence band and the band gap of TiO_2 nanotubes (3.2 eV). The G peak in the visible region originated due to the oxygen vacancies (defects) related trap assisted recombination.

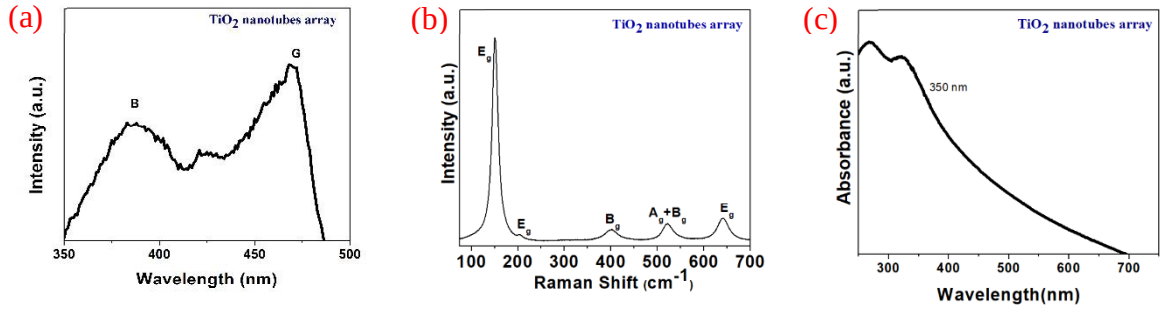

Fig. 2.4. TiO_2 nanotubes array (a) Photoluminescence, (b) Raman spectra (c) UV vis spectra.

Raman spectroscopy is an important tool to study the composition of materials. Raman spectrum of the TiO_2 nanotube array was recorded using a 532 nm laser at room temperature (Fig2.4 (b)). Five peaks were observed in the TiO_2 nanotubes array. The active modes present nearly at 145 cm^{-1} (E_g), 195.4 cm^{-1} (E_g), 395.2 cm^{-1} (B_g), 514.6 cm^{-1} (A_g+B_g) and 634.4 cm^{-1} (E_g) corresponds to the anatase phase of TiO_2 [32],[33].

UV vis spectroscopy for pure TiO_2 nanotubes is represented in Fig. 2.4 (c). UV vis adsorption spectra exhibited the adsorption edge at 350 nm which very well corresponds to the energy band gap (3.2 eV) of TiO_2.

Chemical characterization

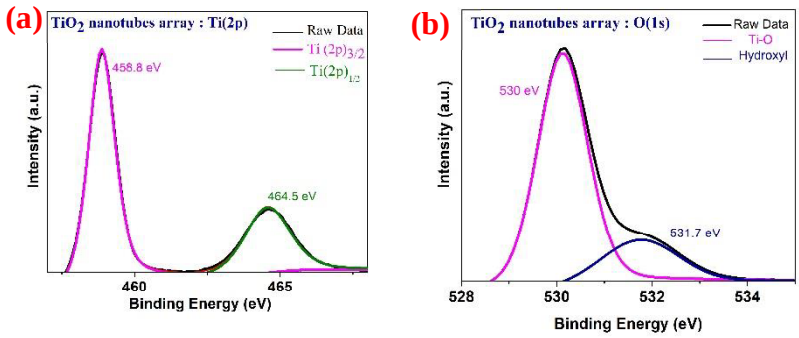

Fig. 2.5. XPS spectra of TiO_2 nanotubes (a) Ti2p, (b) O1s.

Splitting of photoelectrons of Ti^{4+} is assigned to $Ti2p_{3/2}$ and $Ti2p_{1/2}$ with a separation of 5.92 eV that authenticate the existence of anatase TiO_2 (Fig. 2.5(a)) [13].

O1s spectra of TiO_2 nanotubes is deconvoluted into two peaks at 530 eV and 531.7 eV (Fig. 2.5(b)). The high intensity peak at 530 eV corresponds to the lattice oxygen (Ti-O) and small intensity peak at 531.7 eV corresponds to the surface oxygen or adsorbed oxygen [34],[35].

2.3 TiO_2 nanoparticles: 0-D material

2.3.1 Synthesis

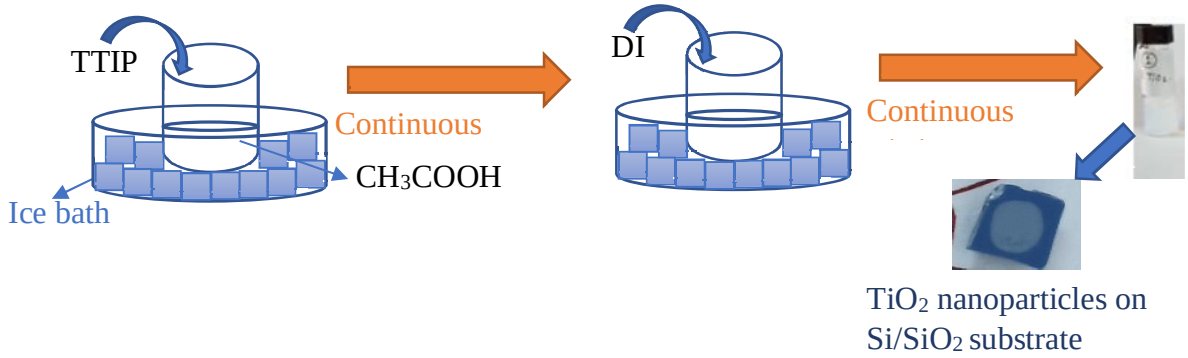

Fig.2.6. Synthesis of undoped *p*-type TiO_2 nanoparticles via sol-gel method.

Undoped *p*-type TiO_2 nanoparticles (NPs) were synthesized by sol-gel method. 2 ml of titanium (IV) iso-propoxide (TTIP, 99.99% pure from Sigma Aldrich) was added dropwise to the 10 ml of acetic acid (CH_3COOH) inside an ice bath under vigorous starting conditions. Then 40 ml of deionized water was added drop wise into the mixture of TTIP and CH_3COOH. The solution was stirred for 90 min and the colour of the solution became completely transparent. Then the TiO_2 solution was aged in a dark place for 48 hours at 20 °C. After aging, the colour of the TiO_2 solution became slightly opaque. Finally, the pure TiO_2 nanoparticle were obtained. Synthesis steps of TiO_2 nanoparticles are represented in Fig. 2.6.

2.3.2 Characterizations

Morphological Characterizations

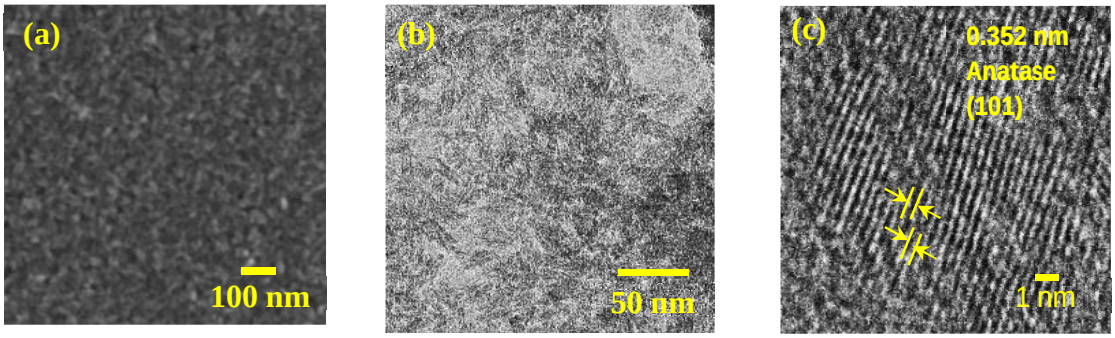

Fig. 2.7. Undoped *p*-type TiO_2 nanoparticles (a) FESEM, (b) TEM, (c) HRTEM representing the lattice fringes.

Uniform, continuous and compact distribution of *p*-TiO_2 NPs is observed in the FESEM image in Fig. 2.7(a). 18 nm average size of TiO_2 NPs was estimated form TEM image in Fig. 2.7(b) and (c). The d-spacing of 0.352 nm measured from lattice image in Fig. 2.7(c) confirmed the formation of anatase (101) crystallinity.

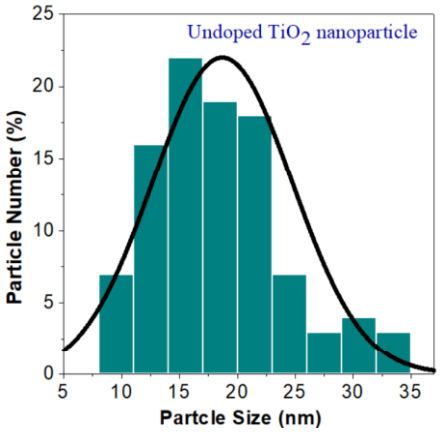

Fig. 2.8. Particle size of undoped *p*-type TiO_2 nanoparticle.

Size of the TiO_2 nanoparticles were varying from 10 to 35 nm with average value of 18 nm as shown in the distribution in Fig. 2.8. Size were estimated from SEM and TEM.

Structural Characterization

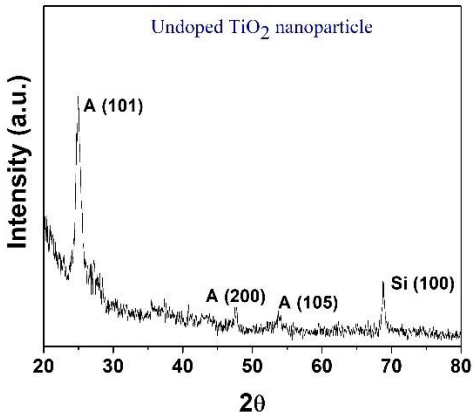

Fig. 2.9. XRD spectrum of undoped *p*-type TiO_2 nanoparticle.

The XRD spectra of undoped TiO_2 nanoparticles is represented in Fig. 2.9. The sharp and high intensity peak at 24.5 ° confirms the anatase crystallinity (101) of TiO_2 nanoparticles. The low intensity peaks at 47.6° and 53.8° correspond to the anatase (200) and (105) respectively. A sharp intensity peak at 68.8° corresponds to the Silicon substrate. The XRD peaks for anatase TiO_2 were authenticated by JCPDS file No. 21-1272.

Other spectroscopic characterizations like PL, Raman and UV vis were carried out to estimate the structural properties of TiO_2 nanoparticles and shown in Fig 2.10(a), (b) and (c) respectively. The photoluminescence spectrum of undoped TiO_2 nanoparticles depicts two peaks- one small B peak in the UV region (320 nm) and another high intensity G peak in the

visible region (520 nm) (Fig. 2.10 (a)). The B peak in the UV region represents direct transition of electron from conduction to the valence band representing the band gap of TiO_2 nanoparticles as 3.6 eV which is also authenticated from the UV vis spectrum of TiO_2 nanoparticles exhibiting the adsorption edge at ~336 nm (Fig. 2.10 (c)). The G peak in the visible region is aroused due to the oxygen vacancies (defects) related trap assisted recombination (Fig. 2.10(a)). The non-stoichiometric nature of TiO_2 nanoparticles with abundant surface oxygen type defects is confirmed by the large intensity G peak at 520 nm (Fig. 2.10 (a)).

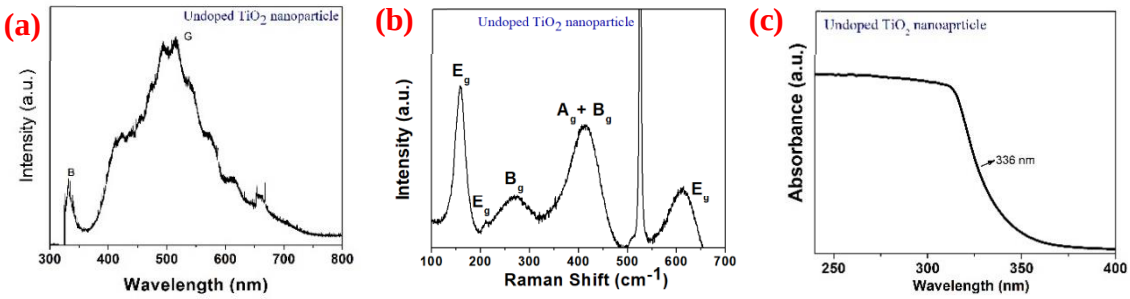

Fig. 2.10. Undoped *p*-type TiO_2 nanoparticles; (a) photoluminescence, (b) Raman, and (c) UV vis spectra.

The presence of anatase crystallinity in *p*-TiO_2 NPs was confirmed by six active Raman modes like E_g (144 cm^{-1}), E_g (199 cm^{-1}), B_g (399 cm^{-1}), $A_g + B_g$ (516 cm^{-1}) and E_g (639 cm^{-1}) (Fig. 2.10 (b)). The high intensity peak at 525 cm^{-1} originated from Si/SiO_2 substrate.

Chemical characterization

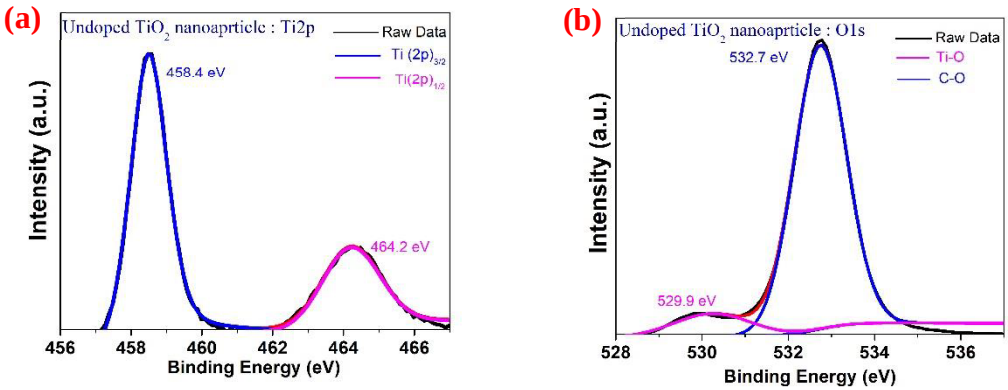

Fig. 2.11. XPS spectra of undoped *p*-type TiO_2 nanoparticles (a) Ti2p, (b) O1s.

Splitting of photoelectrons of Ti^{4+} is assigned to $Ti2p_{3/2}$ and $Ti2p_{1/2}$ with a separation of 5.9 eV that authenticates the existence of anatase TiO_2 Fig. 2.11(a) [13].

O1s spectra of TiO_2 nanoparticles exhibited high intensity peak at 532.8 eV attributed to the surface oxygen originated from Ti-OH, adsorbed oxygen species etc. whereas Ti-O peak intensity at 529.8 eV was quite low (Fig. 2.11(b)) [36]. The high peak intensity at 532.8 eV was observed due to the extremely small dimensions (~12 nm) of the particles that eventually increased the number of surface atoms reducing the bulk formation that results in a high intensity surface oxygen peak compared to the bulk oxygen (Ti-O).

p-type conductivity

Table 2.1 Hall effect result of sol-gel derived undoped *p*-TiO_2 nanoparticles.

Sample Specification	Conductivity	Bulk carrier density	Hall mobility	Bulk resistivity
S_1	*p*-type	8.793×10^{18} cm^{-3}	47 cm^2/Vs	6.462×10^{-6} Ω-cm.
S_2	*p*-type	8.598×10^{18} cm^{-3}	51 cm^2/Vs	3.702×10^{-6} Ω-cm.
S_3	*p*-type	8.461×10^{18} cm^{-3}	63 cm^2/Vs	1.512×10^{-6} Ω-cm.

The Van Der Pauw method was used to confirm the *p*-type conductivity of TiO_2 nanoparticles. The Hall effect measurement was performed with 100 nm current and 0.5 T magnetic field. A set of three samples were synthesized by sol gel technique (under same conditions) for Hall measurement as represented in Table 2.1. The *p*-TiO_2/SiO_2/Si samples with 1 cm ×1 cm dimensions were used for the measurement. Hall measurement determined the p-type conductivity of TiO_2 nanoparticles having carrier concentration around 8.598×10^{18} cm^{-3}, mobility around 51 cm^2/V-s and bulk resistivity around 3.702×10^{-6} Ω-cm.

2.4 Precursor preparation of carbon nanostructures

2.4.1 Synthesis

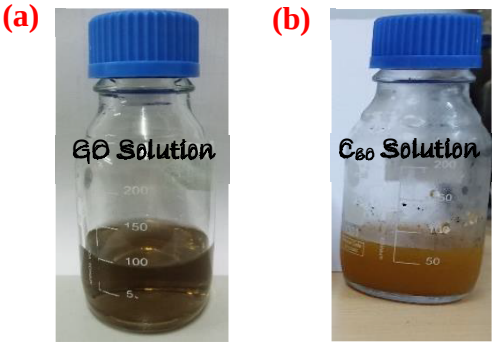

Fig.2.12. (a) 0.2 wt% graphene oxide solution, (b) Fullerene aqueous solution.

Precursor preparation of graphene oxide (2-D material)

Concentrated (6.2 g/L) and aqueous solution of single layer (>80%, flake size: 0.5-5 µm) graphene oxide (GO) of graphene supermarket brand was used. 0.2 wt% stable aqueous solution of GO was used for the further study (Fig 2.12 (a)). 1mg of graphene oxide was added in 500 ml of DI water and solution starred for 15 minutes.

Aqueous solution preparation of fullerene (0-D material)

High purity fullerene C_{60} (Sigma Aldrich, 99.9%) was used to prepare the aqueous solution of fullerene. Firstly, high purity C_{60} fullerene was added to toluene to maintain the concentration around 2 mg/mL and a purple-coloured homogenous mixture was obtained. In the second step the deionized water was added to the precursor solution. Two insoluble phases were formed that were kept for ultrasonication for a long time, until the toluene was evaporated and a yellowish solution was obtained (Fig. 2.12(b)).

2.4.2 Characterization

Morphological characterization

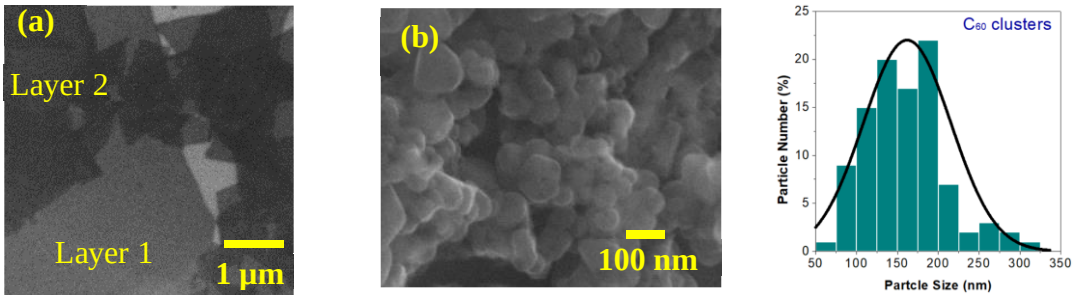

Fig. 2.13. FESEM Image: (a) graphene oxide, (b) fullerene clusters. (c) Size distribution of fullerene clusters obtained from the FESEM image.

FESEM image of graphene oxide (Fig. 2.13(a)) confirms the formation of mostly single or a few layers of GO flakes. C_{60} clusters were spherical in shape (Fig. 2.13(b)). C_{60} clusters of variable sizes (50 nm -350 nm) were observed in FESEM (Fig. 2.13(b)). The size distribution in Fig. 2.13(c) indicates 161 nm of average size of the C_{60} clusters.

Structural characterizations

The graphene oxide depicted the adsorption edge at around 287 nm with a measured band gap around 3.59 eV (Fig. 2.14(a)). C_{60} has two broad absorption edges in the UV region – 216 nm and 224 nm (Fig. 2.14(b)). These optical absorption bands are recognised as dipole allowed transitions in original C_{60} and are accordant with literature [37],[38].

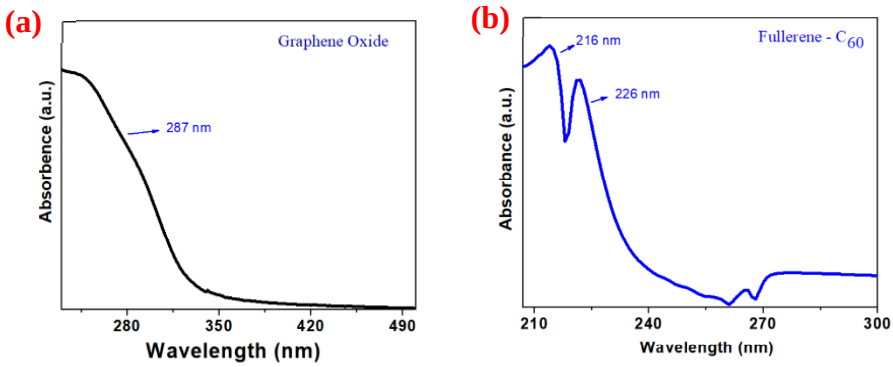

Fig. 2.14. UV vis absorption spectra of (a) graphene oxide, (b) fullerene-C_{60}.

Raman spectroscopy of graphene oxide was performed at room temperature using a 300 nm laser (Fig. 2.15(a)). The two main peaks – D and G at 1300 cm^{-1} and 1600 cm^{-1} were observed in the Raman spectra respectively. D peak contributes to the sp^3 defects in carbon and G peak provides the information of plane vibration in sp^2 configuration [39].

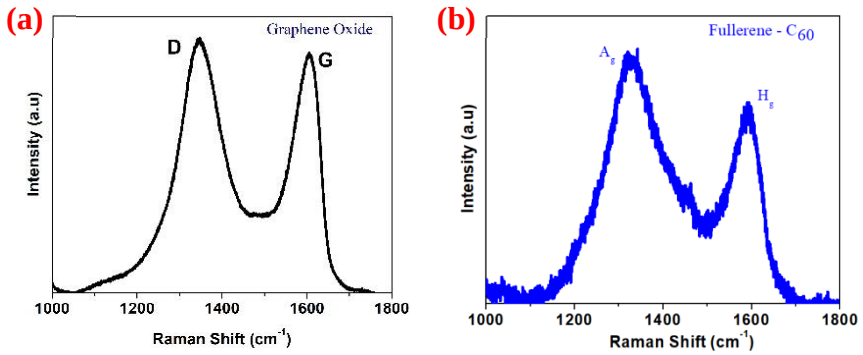

Fig. 2.15. Raman spectra (a) graphene oxide, (b) fullerene.

The calculated I_D/I_G ratio for graphene oxide was 1.05 which very well depicts the lesser number of defects. Similarly, two peaks were observed in fullerene depicting A_g (1) and H_g (8) mode (Fig. 2.15(b)). A_g mode is defined as the pentagonal pinch mode which contributes to C_{60} nanoparticles [38].

Chemical characterization

Strong O1s peak at 532.6 eV originated from pure GO due to presence of oxygen functionalized groups (mainly, hydroxyl/epoxy) on GO surface (Fig. 2.16 (a)) [36]. Similarly, O1s high scan of fullerene depicts a high intensity peak at 532.7 eV corresponding to the adsorbed oxygen groups (C-O, C=O or C-OH) due to the functionalization of fullerene molecules (Fig. 2.16 (c)).

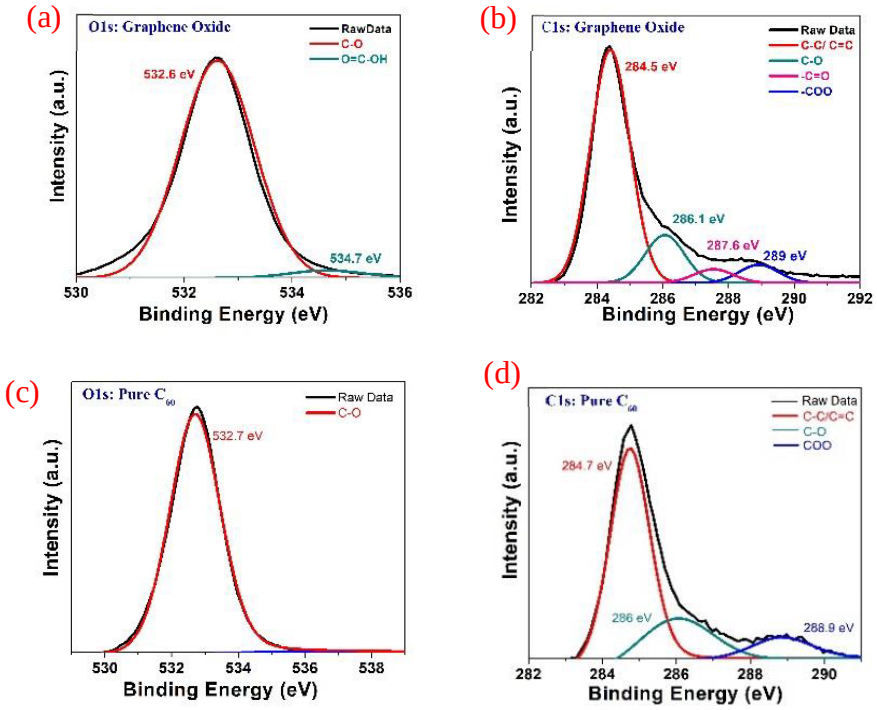

Fig. 2.16. XPS spectra: Graphene oxide with (a) O1s, (b) C1s; Fullerene with (c) O1s, (d) C1s. The high resolution C1s scan of graphene oxide and C_{60} depicted the large intensity peak at 284.5 eV/284.7eV which is attributed to the adventitious carbon and sp^2 hybridization (Fig. 2.16(b) and (d)). Oxygen functionalization such as hydroxyl/epoxy (C-O) peak was located at 286 eV in all the nanocarbons, confirming the good amount of oxidation. The peak located at 287.6 eV corresponds to the carbonaceous band (C=O) in GO The other oxygen functional group like COOH was found for both pure GO and pure C_{60} (Fig. 2.16 (b)) [36],[40].

2.5 Conclusions

Pure TiO_2 nanotubes were prepared by simple electrochemical anodization method and undoped TiO_2 nanoparticles were prepared by sol-gel method. Both the adopted methods were easy and cost effective. Different characterizations including morphological, structural and chemical were performed to analyse the both the TiO_2 nanostructures (nanotube and nanoparticles). FESEM confirmed the formation of highly orientated and organized nanotubes and compact and dense distribution of nanoparticles. XRD confirmed the anatase crystallinity of TiO_2 in both the structures. All the active six modes corresponding to the anatase crystallinity of TiO_2 were observed in Raman spectroscopy of both the nanostructures. X-ray photo spectroscopy was performed to study the composition of TiO_2. TiO_2 nanotubes exhibited *n*-type behaviour and TiO_2 nanoparticles showed *p*-type behaviour.

Pure graphene oxide solution (Graphene supermarket) was synthesized in aqueous form for further use. High purity fullerene (Sigma Aldrich, 99 %) was hydrated to increase its hydrophilicity. Fullerene aqueous solution obtained was highly stable and active. Both pure carbon nanostructures were analysed using different characterization techniques like FESEM, XRD, Raman spectroscopy, UV vis and XPS.

TiO_2 has an advantage of being synthesized in 1-D nanotubes and 0-D nanoparticles where TiO_2 nanostructures have been widely utilized to detect variety of volatile organic compounds (VOCs). Different ways have been adopted by different researchers to improve sensor performance. Out of which one of the way is to enhance the sensing performance of metal oxides is by increasing or decreasing the oxygen vacancy in nanoscale metal oxides which can be considered 'self-doping'.

References

1. P.M. Perillo, D. F. Rodríguez, The gas sensing properties at room temperature of TiO_2 nanotubes by anodization, Sensors and Actuators B: Chemical 171 (2012) 639-643.
2. H. He, Metal oxide semiconductors and conductors, Solution Processed Metal Oxide Thin Films for Electronic Applications (2020) 7.
3. Y. Zheng, L. Zheng, Y. Zhan, X. Lin, Q. Zheng, K. Wei, Ag/ZnO heterostructure nanocrystals: synthesis, characterization, and photocatalysis, Inorganic chemistry 46 17 (2007) 6980-6986.
4. L. Li, J. Huang, T. Wang, H. Zhang, Y. Liu, J. Li, An excellent enzyme biosensor based on Sb-doped SnO_2 nanowires, Biosensors and Bioelectronics 25 11 (2010) 2436-2441.
5. S. Daothong, Characterization of Fe_2O_3 Nanowires and Its Solar Cell Applications, Key Engineering Materials 766 (2018) 217–22.
6. Z. M. Mizwari, Akeem Adeyemi Oladipo, Elvan Yilmaz. Chitosan/metal oxide nanocomposites: synthesis, characterization, and antibacterial activity, International Journal of Polymeric Materials and Polymeric Biomaterials (2020) 1-9.
7. W. Wang, Y. Liu, S. Liu, SnO_2 nanostructure with well-engineered crystal facets by Zn doping for chemical sensing applications, Crystal Growth & Design 20 4 (2020) 2742-2752.
8. J. Su, L. Guo, N. Bao, C. A. Grimes, Nanostructured WO_3/$BiVO_4$ heterojunction films for efficient photoelectrochemical water splitting, Nano letters 11 5 (2011) 1928-1933.

9. S. D. Mo, W. Y. Ching, Electronic and optical properties of three phases of titanium dioxide: Rutile, anatase, and brookite, Physical review B 51 19 (1995) 13023.
10. E. C. Cho, J. H. Ciou, J. H. Zheng, J. Pan, Y. S. Hsiao, K. C. Lee, J. H. Huang, Fullerene C_{70} decorated TiO_2 nanowires for visible-light-responsive photocatalyst, Applied Surface Science 355 (2015) 536-546.
11. S. Riaz, S. J. Park, An overview of TiO_2-based photocatalytic membrane reactors for water and wastewater treatments, Journal of Industrial and Engineering Chemistry 84 (2020) 23-41.
12. S. Colodrero, M. Ocana, H. Míguez, Nanoparticle-based one-dimensional photonic crystals, Langmuir 24 9 (2008) 4430-4434.
13. A. Hazra, B. Bhowmik, K. Dutta, P. P. Chattopadhyay, P. Bhattacharyya, Stoichiometry, length, and wall thickness optimization of TiO_2 nanotube array for efficient alcohol sensing, ACS applied materials & interfaces 7 18 (2015) 9336-9348.
14. J. H. Park, S. Kim, A. J. Bard, Novel carbon-doped TiO_2 nanotube arrays with high aspect ratios for efficient solar water splitting, Nano letters 6 1 (2006) 24-28.
15. Lu, Xihong, Gongming Wang, Teng Zhai, Minghao Yu, Jiayong Gan, Yexiang Tong, and Yat Li. "Hydrogenated TiO2 nanotube arrays for supercapacitors, Nano letters 12 3 (2012) 1690-1696.
16. A. Hazra, S. Das, J. Kanungo, C. K. Sarkar, S. Basu, Studies on a resistive gas sensor based on sol–gel grown nanocrystalline p-TiO_2 thin film for fast hydrogen detection, Sensors and Actuators B: Chemical 183 (2013) 87-95.
17. P. Roy, S. Berger, P. Schmuki, TiO_2 nanotubes: synthesis and applications, Angewandte Chemie International Edition 50 13 (2011) 2904-2939.
18. Y. Li, M. Guo, M. Zhang, X. Wang, Hydrothermal synthesis and characterization of TiO_2 nanorod arrays on glass substrates, Materials Research Bulletin 44 6 (2009) 1232-1237.
19. H. Shin, D. K. Jeong, J. Lee, M. M. Sung, J. Kim. "Formation of TiO_2 and ZrO_2 nanotubes using atomic layer deposition with ultraprecise control of the wall thickness, Advanced Materials 16 14 (2004) 1197-1200.
20. S. Li, G. Zhang, D. Guo, L. Yu, W. Zhang, Anodization fabrication of highly ordered TiO_2 nanotubes, The Journal of Physical Chemistry C 113 29 (2009) 12759-12765.
21. X. Deng, Q. Ma, Y. Cui, X. Cheng, Q. Cheng, Fabrication of TiO_2 nanorods/nanosheets photoelectrode on Ti mesh by hydrothermal method for degradation of methylene blue: influence of calcination temperature, Applied Surface Science 419 (2017) 409-417.

22. N. Kılınš, E. Şennik, Z. Z. ÍztŘrk, Fabrication of TiO_2 nanotubes by anodization of Ti thin films for VOC sensing, Thin Solid Films 520 3 (2011) 953-958.
23. T. Zhai, L. Li, Y. Ma, M. Liao, X. Wang, X. Fang, J. Yao, Y. Bando, D. Golberg, One-dimensional inorganic nanostructures: synthesis, field-emission and photodetection, Chemical Society Reviews 40 5 (2011) 2986-3004.
24. B. Su, Y. Wu, Lei Jiang, The art of aligning one-dimensional (1D) nanostructures, Chemical Society Reviews 41 23 (2012) 7832-7856.
25. Z. Wang, T. Hu, R. Liang, M. Wei, Application of zero-dimensional nanomaterials in biosensing, Frontiers in chemistry 8 (2020) 320.
26. A. Hazra, Partha Bhattacharyya, Tailoring of the gas sensing performance of TiO_2 nanotubes by 1-D vertical electron transport technique, IEEE Transactions on Electron Devices 61 10 (2014) 3483-3489.
27. A. S. Barnard, L. A. Curtiss, Prediction of TiO_2 nanoparticle phase and shape transitions controlled by surface chemistry, Nano letters 5 7 (2005) 1261-1266.
28. A. Hazra, K. Dutta, B. Bhowmik, P. Bhattacharyya, Highly repeatable low-ppm ethanol sensing characteristics of p-TiO_2-based resistive devices, IEEE Sensors Journal 15 1 (2014) 408-416.
29. S. Mao, G. Lu, J. Chen, Nanocarbon-based gas sensors: progress and challenges, Journal of Materials Chemistry A 2 16 (2014) 5573-5579.
30. J. R. Pinzon, A. V. Cerdas, L. Echegoyen, Fullerenes, carbon nanotubes, and graphene for molecular electronics, Unimolecular and Supramolecular Electronics I (2011) 127-174.
31. T. Akita, M. Okumura, K. Tanaka, K. Ohkuma, M. Kohyama, T. Koyanagi, M. Date, S. Tsubota, M. Haruta, Surface and Interface Analysis 37 (2005) 265–269
32. M.J. Šćepanović, M. U. Grujić-Brojčin, Z. D. Dohčević-Mitrović, Z. V. Popović, Effects of confinement, strain and nonstoichiometry on Raman spectra of anatase TiO_2 nanopowders, In Materials Science Forum 518 (2006) 101-106.
33. T. Ohsaka, F. Izumi, Y. Fujiki, Raman spectrum of anatase, TiO_2, Journal of Raman spectroscopy 7 6 (1978) 321-324.
34. Y. Yang, X. Wang, C. Sun, L. Li, Photoluminescence of ZnO nanorod-TiO_2 nanotube hybrid arrays produced by electrodeposition, Journal of Applied physics 105 9 (2009) 094304.

35. S. A. Nasser, X-ray photoelectron spectroscopy study on the composition and structure of BaTiO3 thin films deposited on silicon, Applied surface science 157 1-2 (2000) 14-22.
36. T. Lavanya, K. Satheesh, M. Dutta, N. V. Jaya, N. Fukata, Superior photocatalytic performance of reduced graphene oxide wrapped electrospun anatase mesoporous TiO_2 nanofibers, Journal of alloys and compounds 615 (2014) 643-650.
37. A. Graja, I. Olejniczak, A. Bogucki, D. Bonifazi, F. Diederich, Chromophoric interactions in [60] fullerene–porphyrin dyads investigated by solid-state UV–Vis and IR spectroscopies, Chemical physics 300 1-3 (2004) 227-232.
38. S. Sutradhar, A. Patnaik, A new fullerene-C_{60}–Nanogold composite for non-enzymatic glucose sensing, Sensors and Actuators B: Chemical 241 (2017) 681-689.
39. T. V. Cuong, V. H. Pham, Q. T. Tran, S. H. Hahn, J. S. Chung, E. W. Shin, E. J. Kim. Photoluminescence and Raman studies of graphene thin films prepared by reduction of graphene oxide, Materials letters 64 3 (2010) 399-401.
40. J. Yu, T. Ma, G. Liu, B. Cheng, Enhanced photocatalytic activity of bimodal mesoporous titania powders by C_{60} modification, Dalton Transactions 40 25 (2011) 6635-6644.